Towards Solid-State Magnesium Batteries: Ligand-Assisted Superionic Conductivity

Lasse N. Skov,[a] Jakob B. Grinderslev,[a] Asger Rosenkranz,[a] Young-Su Lee,[b] and Torben R. Jensen*[a]

Solid-state inorganic magnesium batteries are considered as potential high energy storage devices of the future. Here we present a series of magnesium borohydride tetrahydrofuran (THF) composites, $Mg(BH_4)_2 \cdot xTHF(-MgO)$, $0 \leq x \leq 3$, as solid-state electrolytes for magnesium batteries. Three new monoclinic compounds were identified, $Mg(BH_4)_2 \cdot 2/3THF$ (Cc), α-$Mg(BH_4)_2 \cdot 2THF$ ($P2_1/c$) and β-$Mg(BH_4)_2 \cdot 2THF$ ($C2$), and the detailed structures of α- and β-$Mg(BH_4)_2 \cdot 2THF$ are presented. The magnesium ionic conductivity of composites formed by these compounds were several orders of magnitude higher than that of the distinct compounds, $x = 0$, 2/3, 2, and 3. The nanocomposite stabilized by MgO nanoparticles (~ 50 nm),

$Mg(BH_4)_2 \cdot 1.5THF-MgO(75$ wt%), displayed the highest Mg^{2+} conductivity, $\sigma(Mg^{2+}) \sim 10^{-4}$ S cm^{-1} at 70°C, a high ionic transport number of $t_{ion} = 0.99$, and cyclic voltammetry revealed an oxidative stability of ~ 1.2 V vs. Mg/Mg^{2+}. The electrolyte was stable towards magnesium electrodes, which allowed for stable Mg plating/stripping for at least 100 cycles at 55°C with a current density of 0.1 mA cm^{-2}. Finally, a proof-of-concept rechargeable solid-state magnesium battery was assembled with a magnesium metal anode and a TiS_2 cathode. A maximum discharge capacity of 94.2 mAh g^{-1} was displayed, which corresponds to $y = 0.2$ in Mg_yTiS_2.

Introduction

Batteries have become an essential technology in the modern society with a wide range of applications, including portable electronics, electric vehicles and energy storage. Recent estimates predicts a 14-fold increase in the battery market from 180 GWh in 2018 to 2600 GWh in 2030.[1] Advancements within battery performance, such as higher energy density, increased safety, sustainability and lower prices, are essential to meet this huge future demand. Further improvements of the current lithium-ion batteries appear unlikely, and large efforts has been invested in moving away from the currently used graphite anodes, and towards a Li-metal anode to increase the energy density.[2,3] Additionally, the energy density could be improved on battery stack level by replacing the separator and the flammable and hazardous liquid electrolyte with a solid-state inorganic electrolyte, which would also improve the safety.[4]

Utilizing a solid-state electrolyte may result in other benefits such as longer cycle life, less polarization and higher thermal and electrochemical stability.[5,6]

While there are some discussion on how the global lithium reserve can be utilized to meet the future demands,[7,8] the increasing lithium demand has increased prices significantly over the past two decades.[9] In order to decrease the price on batteries, technologies based on more abundant elements, such as magnesium, could be utilized, and can additionally result in an increased energy density.[10] A Mg-metal anode has a high volumetric capacity of 3833 mAh cm^{-3} as compared to Li-graphite and Li-metal of 760 mAh cm^{-3} and 2046 mAh cm^{-3}, respectively.[11]

Due to the divalent nature and strong interaction of the Mg^{2+}-ion with solid matter, there are only few reports of magnesium-based solid-state electrolytes. A good solid-state electrolyte should have a high Mg^{2+} conductivity at moderate temperatures, that also allows Mg plating/stripping on the Mg-anode and enables insertion of Mg^{2+} into the cathode-material.[12] Complex hydride-based electrolytes has emerged as a promising class of superionic conductors and may offer several advantages in terms of compatibility with metal anodes, high gravimetric energy densities, and a good interfacial contact and easy manufacturing due to a high deformability.[13–17] While $Mg(BH_4)_2$ is a poor solid-state conductor with a low ionic conductivity of $\sigma(Mg^{2+}) < 10^{-12}$ S cm^{-1} at $T = 30$°C,[18] recent work has demonstrated a several order of magnitude increase in the Mg^{2+} conductivity by introducing a neutral ligand.

This new class of superionic conductors was initiated by the discovery of ethylediamine (en) derivatives of magnesium borohydride, $Mg(BH_4)_2 \cdot NH_2(CH_2)_2NH_2$, which showed a high

[a] L. N. Skov, Dr. J. B. Grinderslev, A. Rosenkranz, Prof. T. R. Jensen
Interdisciplinary Nanoscience Center (iNANO)
and Department of Chemistry
Aarhus University, Langelandsgade 140,
8000 Aarhus C, Denmark
E-mail: trj@chem.au.dk
[b] Dr. Y.-S. Lee
Energy Materials Research Center,
Korea Institute of Science and Technology,
Seoul 02792, Republic of Korea

Batteries & Supercaps

Research Article
doi.org/10.1002/batt.202200163

Chemistry Europe
European Chemical
Societies Publishing

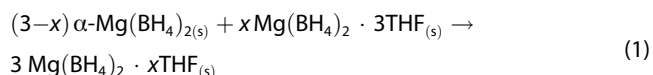Mg^{2+} conductivity of $\sigma(Mg^{2+}) = 6 \times 10^{-5}\,S\,cm^{-1}$ at $T = 70\,°C$ and demonstrated reversible plating/stripping and an oxidative stability of $\sim 1.2\,V$ on Pt vs. Mg/Mg^{2+} in a two electrode setup.[18] Later, other neutral ligands such as diglyme (dg) was also investigated with a slightly lower ionic conductivity of $\sigma(Mg^{2+}) = 2 \times 10^{-5}\,S\,cm^{-1}$ at $T \sim 80\,°C$ for $Mg(BH_4)_2 \cdot \frac{1}{2}dg$.[19] A study of a magnesium borohydride ammonia borane complex, $Mg(BH_4)_2 \cdot 2NH_3BH_3$, revealed a significantly higher conductivity of $\sigma(Mg^{2+}) = 5.0 \times 10^{-6}\,S\,cm^{-1}$ at $T = 25\,°C$, but with a low melting point of $T \sim 47\,°C$.[20,21] The ammine derivatives, $Mg(BH_4)_2 \cdot xNH_3$ ($x = 1, 2, 3, 6$) has also been investigated, and the highest conductivity was found for $x = 1$ with $\sigma(Mg^{2+}) = 3.3 \times 10^{-4}\,S\,cm^{-1}$ at $T = 80\,°C$, which was subjected to detailed studies by density functional theory (DFT) calculations to elucidate the conduction mechanism.[22] A versatile BH_4^- coordination, a relatively free exchange of NH_3 between the framework and migrating cation and a flexible structure was found to be important for the high conductivity in these compounds.[22–24] A follow-up study revealed that ionic conductivity could be further enhanced by forming a nano-composite and the highest conductivity was observed for $Mg(BH_4)_2 \cdot 1.6NH_3$, with an ionic conductivity of $\sigma(Mg^{2+}) = 3.5 \times 10^{-4}\,S\,cm^{-1}$ at $T = 50\,°C$.[25,26] This composite, consisting of $Mg(BH_4)_2 \cdot 1NH_3$ (40%) and $Mg(BH_4)_2 \cdot 2NH_3$ (60%), was further stabilized by MgO nanoparticles, which increased the room temperature conductivity from $\sigma(Mg^{2+}) = 1.9 \times 10^{-8}$ to $\sigma(Mg^{2+}) = 2.2 \times 10^{-6}\,S\,cm^{-1}$.[25]

Here we report the synthesis, structural, thermal- and electrochemical properties of a series of magnesium borohydride tetrahydrofuran composites, $Mg(BH_4)_2 \cdot xTHF$; $0 \leq x \leq 3$, which show promise as materials for solid-state magnesium electrolytes. We characterize the previously reported $Mg(BH_4)_2 \cdot 3THF$,[27] along with three new compounds identified from temperature-varied in situ synchrotron radiation powder X-ray diffraction (SR-PXD), α- and β-$Mg(BH_4)_2 \cdot 2THF$ and $Mg(BH_4)_2 \cdot 2/3THF$, and evaluate their ionic conductivity. Furthermore, composites obtained from mixing these compounds demonstrate several orders of magnitude higher ionic conductivity. These are subjected to further electrochemical investigations, demonstrating a high coulombic efficiency as determined from cyclic voltammetry (CV) and a good Mg-metal anode compatibility as determined from galvanostatic cycling (GC) in a symmetric Mg cell.

Results and Discussion

Synthesis and initial analysis

A series of magnesium borohydride tetrahydrofuran, $Mg(BH_4)_2 \cdot xTHF$, was synthesized and characterized as solid-state electrolytes for Mg-batteries. The samples were synthesized mechano-chemically by reacting solid and crystalline α-$Mg(BH_4)_2$ and $Mg(BH_4)_2 \cdot 3THF$ in appropriate ratios according to Equation (1):

$$(3-x)\,\alpha\text{-}Mg(BH_4)_{2(s)} + x\,Mg(BH_4)_2 \cdot 3THF_{(s)} \rightarrow$$
$$3\,Mg(BH_4)_2 \cdot xTHF_{(s)} \tag{1}$$

The samples with composition $0 < x \leq 2$ were relatively soft, and mechanical stabilization was necessary to prevent both deformation and short circuit during the electrochemical measurements. The mechanical stabilization was achieved by the addition of insulating and inert magnesium oxide, MgO ($\sim$ 50 nm), nanoparticles in appropriate amounts (60–75 wt%). For the compound $Mg(BH_4)_2 \cdot 2THF$, 60 wt% MgO was sufficient for mechanical stabilization, while a higher content of 75 wt% MgO was necessary for the softer composites $0 < x < 2$. The resulting nano-composites are solid powdered samples, which are considered here as the solid electrolyte. An overview of investigated samples and their composition are provided in Table 1.

All samples were initially investigated using SR-PXD (Figure 1). The data reveals diffraction from four distinct compounds of $Mg(BH_4)_2 \cdot xTHF$ with the compositions $x = 0$, 2/3, 2 and 3, where all additional samples are mixtures of these compounds and MgO. Two set of Bragg diffraction peaks can be assigned to the known compounds α-$Mg(BH_4)_2$ and $Mg(BH_4)_2 \cdot 3THF$. $Mg(BH_4)_2 \cdot 3THF$ crystallizes in the monoclinic space group $C2/c$ and has been described previously.[27] Two new compositions have been identified in this work, where one exists with two polymorphic structures, α- and β-$Mg(BH_4)_2 \cdot 2THF$ and the other is $Mg(BH_4)_2 \cdot 2/3THF$. Structural solution of the latter was not successful, but indexing suggests a monoclinic unit cell with space group symmetry Cc, with a Wyckoff site multiplicity of 4. The composition can be estimated from Equation (2):

Table 1. Investigated samples and their composition.

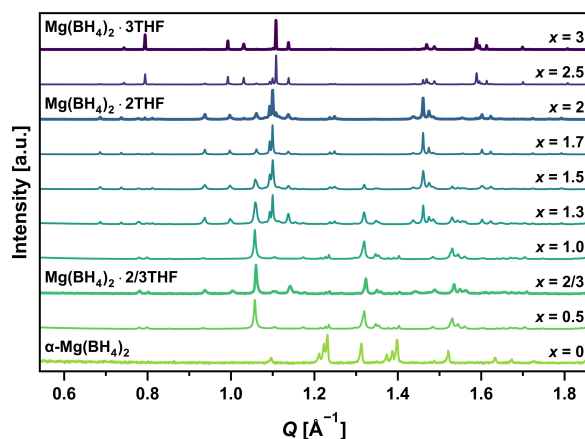| Sample name	Average composition	Crystalline components	MgO [wt%]
$x = 3.0$	$Mg(BH_4)_2 \cdot 3.0THF$	$Mg(BH_4)_2 \cdot 3.0THF$	0
$x = 2.5$	$Mg(BH_4)_2 \cdot 2.5THF$	$Mg(BH_4)_2 \cdot 3.0THF$, $Mg(BH_4)_2 \cdot 2.0THF$	0
$x = 2.0$	$Mg(BH_4)_2 \cdot 2.0THF$	$Mg(BH_4)_2 \cdot 2.0THF$	0
$x = 2.0$	$Mg(BH_4)_2 \cdot 2.0THF$	α-$Mg(BH_4)_2 \cdot 2.0THF$ (87%), β-$Mg(BH_4)_2 \cdot 2.0THF$ (13%), MgO	60
$x = 1.7$	$Mg(BH_4)_2 \cdot 1.7THF$	$Mg(BH_4)_2 \cdot 2.0THF$, $Mg(BH_4)_2 \cdot 2/3THF$, MgO	75
$x = 1.5$	$Mg(BH_4)_2 \cdot 1.5THF$	$Mg(BH_4)_2 \cdot 2.0THF$, $Mg(BH_4)_2 \cdot 2/3THF$, MgO	50
$x = 1.5$	$Mg(BH_4)_2 \cdot 1.3THF$	$Mg(BH_4)_2 \cdot 2.0THF$, $Mg(BH_4)_2 \cdot 2/3THF$, MgO	75
$x = 1.3$	$Mg(BH_4)_2 \cdot 1.3THF$	$Mg(BH_4)_2 \cdot 2.0THF$, $Mg(BH_4)_2 \cdot 2/3THF$, MgO	75
$x = 1.0$	$Mg(BH_4)_2 \cdot 1.0THF$	$Mg(BH_4)_2 \cdot 2.0THF$, $Mg(BH_4)_2 \cdot 2/3THF$	0
$x = 1.0$	$Mg(BH_4)_2 \cdot 1.0THF$	$Mg(BH_4)_2 \cdot 2.0THF$, $Mg(BH_4)_2 \cdot 2/3THF$, MgO	75
$x = 2/3$	$Mg(BH_4)_2 \cdot 2/3THF$	$Mg(BH_4)_2 \cdot 2/3THF$, MgO	75
$x = 0.5$	$Mg(BH_4)_2 \cdot 0.5THF$	$Mg(BH_4)_2 \cdot 2/3THF$, α-$Mg(BH_4)_2$, MgO	75
$x = 0$	$Mg(BH_4)_2$	α-$Mg(BH_4)_2$	0

Figure 1. Normalized SR-PXD data measured at RT of the series of Mg-$(BH_4)_2 \cdot x$THF ($0 \leq x \leq 3$). The data are shown for a limited Q-range to avoid the dominating reflections from MgO.

$$V/Z(Mg(BH_4)_2 \cdot x\text{THF}) \approx V/Z(Mg(BH_4)_2) + x \cdot V/Z(\text{THF}), \quad (2)$$

where V is the unit cell volume and Z is the number of formula units (Figure S1). This suggests that $Z = 12$ with a composition of Mg(BH$_4$)$_2 \cdot$2/3THF, in accord with the amount of reactants used for the synthesis. The volume of each THF in Mg-(BH$_4$)$_2 \cdot x$THF is determined from the slope to ~ 117 Å^3, agreeing well with the volume from solid THF (~ 101 Å^3). Crystallographic data of the compounds investigated here are presented in Table 2 and Rietveld refinements are shown in Figures S2–S5.

All samples contain crystalline Mg(BH$_4$)$_2 \cdot x$THF ($x = 2/3$, 2, or 3), but the softness of the composites formed between two Mg(BH$_4$)$_2 \cdot x$THF with different x-values suggest that some domains in the structure are in an amorphous liquid-like state,

e.g., on the surface of the MgO nanoparticles. A similar phenomenon was observed for Mg(BH$_4$)$_2 \cdot x$NH$_3$ mixed with MgO or Al$_2$O$_3$ nanoparticles, where a eutectic molten state was stabilized on the surface of the nanoparticles, forming a solid nanocomposite.[25,26] This resulted in an increase in Mg^{2+} conductivity by several orders of magnitude.

Crystal structure analysis

α-Mg(BH$_4$)$_2 \cdot$2THF crystallizes in the monoclinic space group $P2_1/c$ and consists of molecular tetrahedral complexes of [Mg(BH$_4$)$_2$(THF)$_2$], where THF coordinates through the lone pair on O (Figure 2a). The Mg–B distances are 2.31 and 2.60 Å, suggesting that the shorter bond corresponds to tridentate BH$_4^-$ (κ^3) and the longer to bidentate (κ^2) coordination, which is supported by the DFT calculations. The Mg–O bond distances are 1.85 and 1.90 Å, which are slightly shorter compared to those in Mg(BH$_4$)$_2 \cdot$3THF, i.e. 2.07 to 2.10 Å.[27]

β-Mg(BH$_4$)$_2 \cdot$2THF is observed in minor amounts in the as-synthesized $x = 2$ sample, but appears to be a high temperature polymorph as it is formed from α-Mg(BH$_4$)$_2 \cdot$2THF during heating at $T > 70$°C. In accord with the experimental observation, DFT calculations finds that β-Mg(BH$_4$)$_2 \cdot$2THF is slightly higher in energy than α-Mg(BH$_4$)$_2 \cdot$2THF (Table S1). β-Mg-(BH$_4$)$_2 \cdot$2THF crystallizes in the monoclinic space group $C2$ and also consists of molecular tetrahedral complexes of [Mg-(BH$_4$)$_2$(THF)$_2$], with a similar local structure as the α-polymorph, but with a rotation of one of the THF molecules relative to the other (Figure 2b). The Mg–B distances are 2.27 and 2.49 Å, consistent with a tridentate (κ^3) and bidentate (κ^2) BH$_4^-$ coordination. The Mg–O bond distances are 1.98 and 2.10 Å, which are similar to those observed in Mg(BH$_4$)$_2 \cdot$3THF.[27]

Table 2. Crystallographic data extracted from the SR-PXD data shown in Figure 1 using Rietveld refinement (see Figures S2–S5).

Compound	Space group	a [Å]	b [Å]	c [Å]	β [°]	V [Å^3]	T [°C]
Mg(BH$_4$)$_2 \cdot$3THF[a]	$C2/c$	12.1971(5)	12.6779(4)	20.349(1)	145.248(2)	1793.6(1)	22
α-Mg(BH$_4$)$_2 \cdot$2THF	$P2_1/c$	7.789(1)	10.908(1)	17.127(2)	90.428(5)	1455.2(3)	22
β-Mg(BH$_4$)$_2 \cdot$2THF	$C2$	11.9563(4)	11.0893(4)	10.9966(4)	95.5410(9)	1451.19(9)	70
Mg(BH$_4$)$_2 \cdot$2/3THF[b]	Cc	13.6253(8)	9.6516(9)	16.329(1)	100.296(2)	2112.8(3)	-23

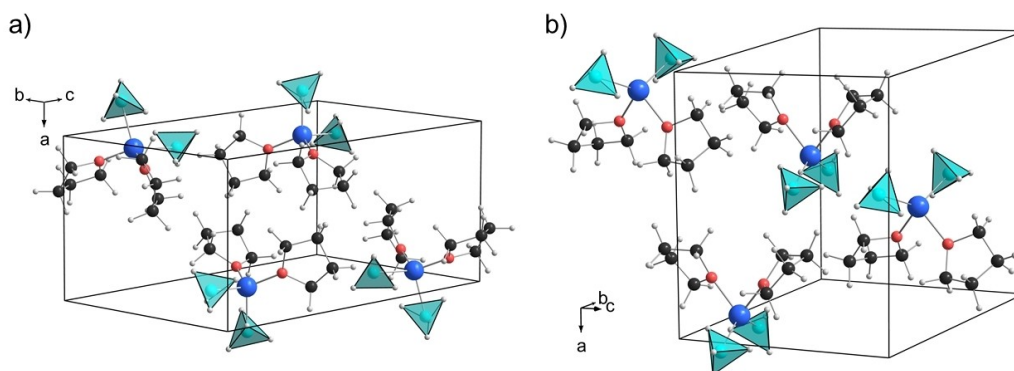[a] Structure solved in Ref. [27], [b] The detailed crystal structure remains unknown.

Figure 2. Crystal structure of a) α-Mg(BH$_4$)$_2 \cdot$2THF ($P2_1/c$) and b) β-Mg(BH$_4$)$_2 \cdot$2THF ($C2$). Color scheme: Mg (blue), B (cyan), O (red), C (black) and H (grey).

Batteries & Supercaps

Research Article
doi.org/10.1002/batt.202200163

Chemistry Europe
European Chemical
Societies Publishing

Thermal analysis

The thermal stability of the distinct compounds $Mg(BH_4)_2 \cdot xTHF$, $x = 2/3, 2, 3$, were investigated with simultaneous thermogravimetry, differential scanning calorimetry and mass spectrometry (TG-DSC-MS) (Figure S6) and in situ SR-PXD (Figure S7). TG-DSC-MS of $x = 3$ showed that THF was released in two distinct events, where an initial release of THF in the temperature range from 30 to 90 °C resulted in an observed mass loss of ~26.2 wt %, corresponding to the release of one THF ($\Delta m/m$(calc) = 26.7 wt%). A second release of THF occurs in the temperature range from 90 to 200 °C, accompanied by a small amount of hydrogen affording a total mass loss of ~34 wt%, suggesting a release of 4/3 THF ($\Delta m/m$(calc) = 35.6 wt%). This agrees well with the formation of $Mg(BH_4)_2 \cdot 2THF$ and $Mg(BH_4)_2 \cdot 2/3THF$ during heating. In situ SR-PXD data show that $Mg(BH_4)_2 \cdot 3THF$ melts and becomes amorphous at $T \sim 80$ °C (Figure S7c), while α-$Mg(BH_4)_2 \cdot 2THF$ shows a polymorphic transition to β-$Mg(BH_4)_2 \cdot 2THF$ at $T \sim 70$ °C, followed by melting at $T \sim 80$ °C (Figure S7b). $Mg(BH_4)_2 \cdot 2/3THF$ melts at $T \sim 80$ °C (Figure S7a). The melting is associated with an increasing background intensity. Thus, the $Mg(BH_4)_2 \cdot 2THF$ and $Mg(BH_4)_2 \cdot 2/3THF$ formed during heating of $Mg(BH_4)_2 \cdot 3THF$ is in a molten state. Interestingly, the TG-DSC-MS data of $Mg(BH_4)_2 \cdot 3THF$ (Figure S6c) indicates that $Mg(BH_4)_2 \cdot 2/3THF$ is stable up to 200 °C, but the TG-DSC-MS data of $x = 2.0$ (60 wt% MgO) and $x = 2/3$ (75 wt% MgO) shows the release of ~2 THF ($\Delta m/m$(calc) = 29.1 wt%) and ~2/3 THF ($\Delta m/m$(calc) = 11.8 wt%) and minor amounts of H_2 in the temperature range 120 to 240 °C, suggesting that the MgO nanoparticles may significantly lower the THF release temperature (Figure S6a).

The highest magnesium ionic conductivity is observed for $Mg(BH_4)_2 \cdot 1.5THF$–MgO(75 wt%) (see Section 2.4), which has sufficient mechanical stability to be considered a functional battery material, and was subject to further thermal analysis, see Figure 3. In situ SR-PXD shows that the diffraction from $Mg(BH_4)_2 \cdot 2THF$ and $Mg(BH_4)_2 \cdot 2/3THF$ decreases in intensity from 55 °C and disappears above 65 °C, which is assigned to a eutectic melting of $Mg(BH_4)_2 \cdot 1.5THF$ (Figure 3a). Above 65 °C, diffraction is only observed from MgO (Figure S8). A total mass loss of 12.5% in the temperature range from 60 to 200 °C, corresponding to the release of 0.5 THF ($\Delta m/m$(calc) ~ 12.7 wt %), was detected by TG-MS (Figure 3b), and a pellet of the sample was found to be mechanically stable without any visual changes upon heating to 150 °C (Figure 3c).

Magnesium ionic conductivity

The temperature-dependent magnesium ionic conductivity was measured for the $Mg(BH_4)_2 \cdot xTHF$–MgO composites ($x = 2/3, 1.0, 1.3, 1.5, 1.7, 2.0$) with EIS (Figure 4a). The composites from the distinct compounds, $x = 2/3$ and 2.0, were found to have conductivities in the order of 10^{-7} S cm^{-1} at $T = 70$ °C. By mixing the distinct compounds to obtain the average compositions $x = 1.0, 1.3, 1.5, 1.7$, a several orders of magnitude increase in the ionic conductivity was achieved. The steep slope (high activation energy) during the initial heating of the composites with $x = 1.5, 1.7, 2.0$, decrease significantly in the following cycles. This is explained by the elimination of the grain boundaries, and a considerably higher ionic conductivity is achieved during the second heating (Figure S9a). The highest ionic conductivity of the series was found for $x = 1.5$, $\sigma(Mg^{2+}) = 1.7 \times 10^{-4}$ S cm^{-1} at $T = 70$ °C and $\sigma(Mg^{2+}) = 9.8 \times 10^{-7}$ S cm^{-1} at $T = 30$ °C after heating. The Nyquist and Bode plots for $x = 1.5$ from 30 to 70 °C are shown in supporting information (Figure S10). The activation energy for $Mg(BH_4)_2 \cdot 1.5THF$–MgO(75 wt%) was evaluated from the second
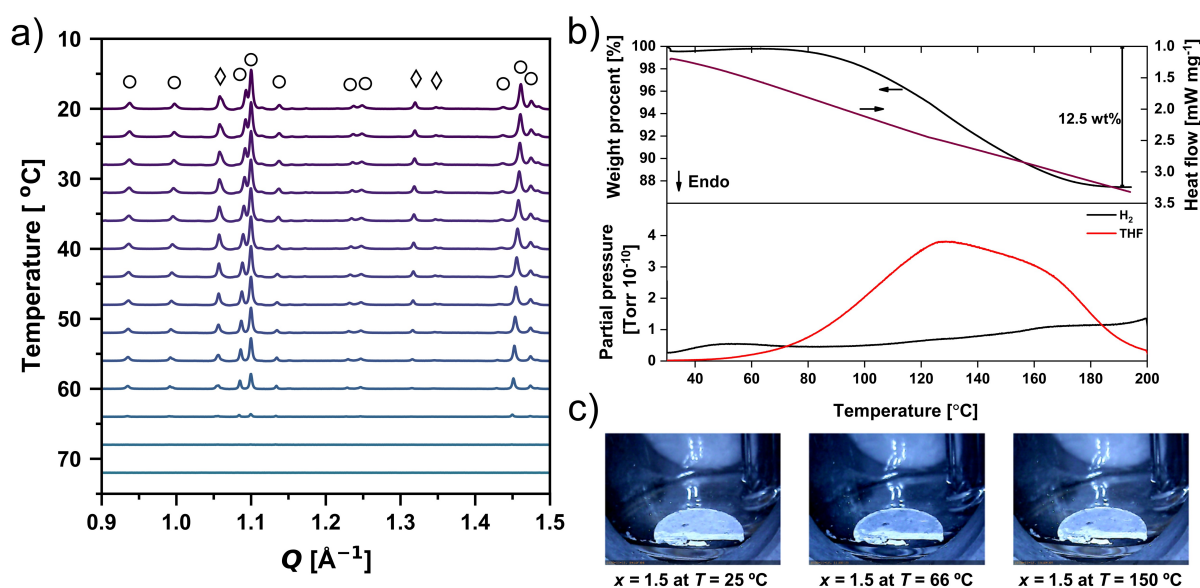

Figure 3. Thermal analysis of the composite $Mg(BH_4)_2 \cdot 1.5THF$–MgO(75 wt%). a) In situ SR-PXD data from 20 to 75 °C ($\Delta T/\Delta t = 5$ °C min^{-1}). The data is shown for a limited Q-range to avoid the dominating reflections from MgO. Markers ($\diamond$) and ($\bigcirc$) represent reflections for $Mg(BH_4)_2 \cdot 2/3THF$ and $Mg(BH_4)_2 \cdot 2THF$, respectively. b) Combined TG-DSC-MS measurements ($\Delta T/\Delta t = 0.5$ °C min^{-1}). c) In situ photographic analysis of a pellet during heating at 25, 66 and 150 °C.
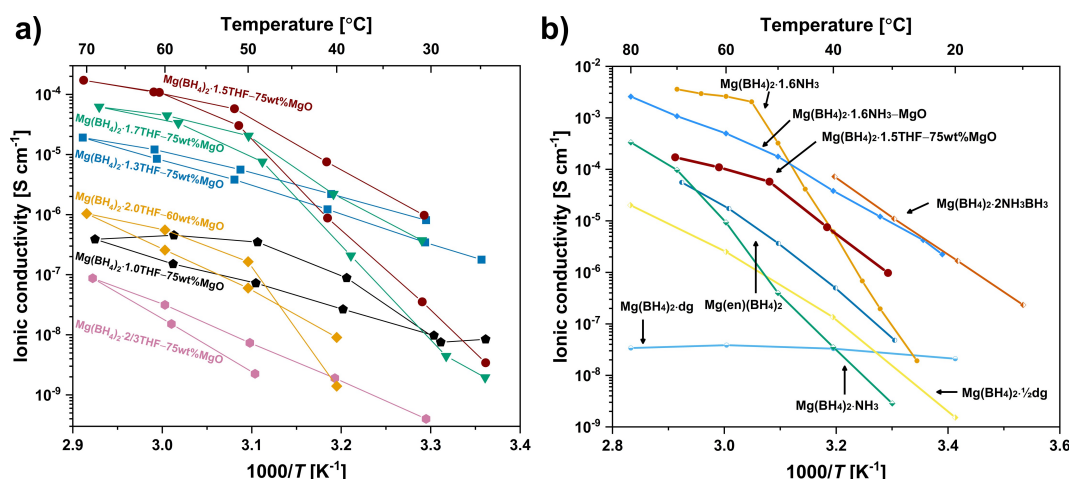
Batteries & Supercaps

Research Article
doi.org/10.1002/batt.202200163

Chemistry Europe
European Chemical
Societies Publishing

Figure 4. a) Temperature-dependent Mg^{2+} ionic conductivity of $Mg(BH_4)_2 \cdot x$THF ($x = 2/3$, 1.0, 1.3, 1.5, 1.7, 2.0). b) Mg^{2+} conductivity of $x = 1.5$ compared to other fast Mg-ion conductors at temperatures below 100 °C.[18,19,21,22,25]

heating ramp in the temperature range from 30 to 60 °C from a $\ln(\sigma\,T)$ versus $1/T$ plot (Figure S9d). The activation energy of $E_a = 1.4$ eV is in the same range as other magnesium borohydride-based compounds.[21,25]

Mixing two distinct compounds, e.g., $Mg(BH_4)_2 \cdot 2/3$THF and $Mg(BH_4)_2 \cdot 2$THF, to increase the ionic conductivity has also been observed for the ammine magnesium borohydride analogues, $Mg(BH_4)_2 \cdot x$NH$_3$.[25] A composite, $Mg(BH_4)_2 \cdot 1.5$NH$_3$, is eutectic melting ($T \sim 55$ °C) and was stabilized by MgO nanoparticles. Interestingly, solid-state ^{11}B NMR revealed that the dynamics of the molten state was stabilized in a mechanically stable solid to low temperatures (below RT) for prolonged time (> months). The large surface area nano-additive (MgO) nanoconfined the molten state and prevented crystallization and thereby preserved the high ionic conductivity.[25,26] Here a similar phenomenon is observed using the neutral THF molecule, forming composites of stoichiometric compounds, which are stabilized by large surface area, inert and insulating nano-particles. In comparison with other known magnesium ionic conductors, $Mg(BH_4)_2 \cdot 1.5$THF—MgO(75 wt%) exhibits among the highest reported conductivities below 100 °C (Figure 4b), only exceeded by the $Mg(BH_4)_2 \cdot x$NH$_3$ and $Mg(BH_4)_2 \cdot 2$NH$_3$BH$_3$ systems (Figure 4b).[21,25]

A relatively high MgO content was necessary to ensure sufficient mechanical stability, but also affects the ionic conductivity. The samples of $Mg(BH_4)_2 \cdot x$THF with $x = 1.0$, 2.0, 3.0, without MgO display both a lower ionic conductivity and lower mechanical stability as compared to the samples containing 75 wt% MgO (Figure S9c). The $Mg(BH_4)_2 \cdot 1.5$THF composite was investigated with 50 wt% MgO, and due to the soft nature of the pellet, the conductivity was measured in an electrochemical cell (PEEK cell) with a fixed volume (Figure S9b). This composite reached an ionic conductivity of 9.8×10^{-3} S cm^{-1} at $T = 70$ °C, suggesting that the high MgO content of 75 wt% lowers the ionic conductivity, but is necessary for mechanical stabilization. Thus, the ionic conductivity can likely be further optimized by using other and smaller nanoparticles

with a larger surface area in smaller amounts, while retaining mechanical stability.

Electrochemical characterization

The electrochemical stability of $Mg(BH_4)_2 \cdot 1.5$THF—MgO(75 wt%) was evaluated with CV at $T = 55$ °C in a two-electrode setup with a stainless steel (SS) working electrode and Mg as a counter/reference electrode (Figure 5a). At this temperature, the Mg^{2+} conductivity is sufficiently high and it is well below the temperature for release of THF. The voltage was initially scanned between −0.25 to 1.25 V with a scan rate of 5 mV s^{-1} for 100 cycles. An anodic current begins to flow at ~1.2 V vs. Mg/Mg^{2+}, indicating an oxidation of the electrolyte above this voltage. The oxidation becomes less apparent as a function of cycles suggesting the formation of a stable interface that allow plating and stripping of magnesium. The plating and stripping of magnesium on the SS-electrode can be observed below and above 0 V, respectively. On the first cycle, a large overvoltage is present, and as the forward scan starts after reaching the switch voltage, the plating current continues with a constant current < −0.2 V, indicating a surface activation of the electrodes. It has to be noted that these phenomena cannot be exclusively ascribed to an individual electrode in a two-electrode setup. On subsequent cycles, the overvoltage decreases and the plating exhibited a linear current increase as would be expected from Mg-plating. The surface activation can also be seen in the coulombic efficiency, which was 37.5% on the first cycle, but increased to 89.6% at cycle 50 (Figure 5a inset). It has previously been reported that Mg-metal has to be activated electrochemically to lower the interfacial impedance, as is also suggested for the $Mg(BH_4)_2 \cdot 1.5$THF system.[28] In comparison, the liquid electrolyte analogue, $Mg(BH_4)_2$ (0.5 M) in THF has a lower coulombic efficiency of 40%.[29] Thus, the advantage of $Mg(BH_4)_2 \cdot 1.5$THF—MgO(75 wt%) is a larger density of charge carriers, which increases the coulombic efficiency after activation.

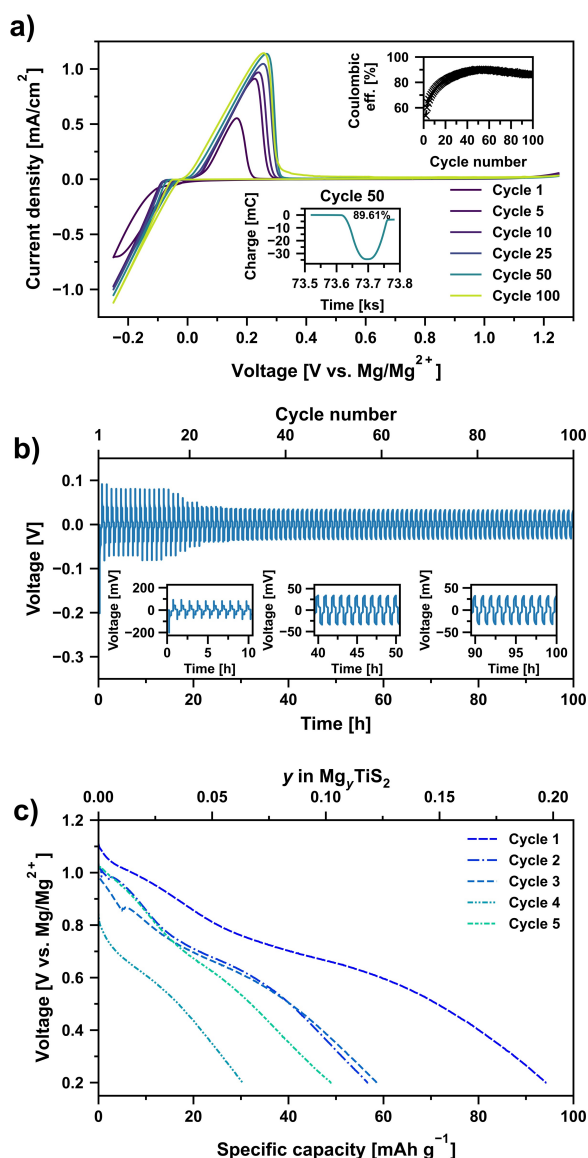**Figure 5.** a) Cyclic voltammetry of the $Mg(BH_4)_2 \cdot 1.5THF–MgO(75\ wt\%)$ composite at 55 °C, with stainless-steel as the working electrode and Mg as the counter/reference electrode in a two electrode setup, using a scan rate of 5 mV s^{-1}. Inset (top) shows the coulombic efficiency as a function of cycle number. Inset (bottom) is the charge transferred during the plating/stripping in cycle 50. b) Galvanostatic cycling of a symmetric $Mg|Mg$-$(BH_4)_2 \cdot 1.5THF–MgO(75\ wt\%)|Mg$ cell at $T=55$ °C with a constant current density of 0.1 mA cm^{-2}. c) Galvanostatic cycling (C/50) of $TiS_2|Mg$-$(BH_4)_2 \cdot 1.5THF–MgO(75\ wt\%)|Mg$ at $T=55$ °C.

After 100 cycles, the voltage range was expanded to 1.8 V, but a stable plating/stripping was still observed (Figure S11a). The oxidative current at > 1.2 V decreases upon cycling, which is also observed for the plating/stripping current, indicating an interface formation that inhibits Mg^{2+} migration. This Mg^{2+} inhibiting interface becomes more evident as the voltage range was further increased after cycle 150, first to 3.4, 4.0 and then 4.4 V in the subsequent cycles (Figure S11b). The expanded voltage range reveals three oxidative processes with peak potentials around 2.5, 3.2 and 4.3 V, respectively. After cycle 151, the plating and stripping currents around 0 V are

drastically reduced, indicating the formation of a magnesium plating/stripping inhibiting interface at these voltages.

The compatibility of the electrolyte Mg-$(BH_4)_2 \cdot 1.5THF–MgO(75\ wt\%)$ with a Mg metal anode was demonstrated by galvanostatic cycling of a symmetric $Mg|Mg(BH_4)_2 \cdot 1.5THF–MgO(75\ wt\%)|Mg$ cell at $T=55$ °C (Figure 5b). The cell was cycled for 100 cycles before terminating the experiment with a current density of 0.1 mA cm^{-2} in steps of 15 min positive and negative applied current with 15 min rest in between. A large initial polarization was present in the first cycles, which decreases to a steady plating/stripping. This illustrates a good anode compatibility of the electrolyte and indicates the above-mentioned surface activation.[28]

Additionally, CV and GC was measured for Mg-$(BH_4)_2 \cdot xTHF–MgO(75\ wt\%)$ $(x=1.3)$ to ensure that the electrochemical parameters were not sensitive to a specific x-value (Figure S12). The coulombic efficiency for the $x=1.3$ composite was evaluated to 86 % at cycle 20 (Figure S12a inset). Note that differences in the current density and polarization from $x=1.3$ and 1.5 are due to differences in pellet thickness. Likewise, a stable plating and stripping for > 500 cycles was measured. For $Mg(BH_4)_2 \cdot 1.3THF–MgO(75\ wt\%)$, the ionic transport number was estimated from Equation 3 using a symmetric cell with SS blocking electrodes. The monitored peak current (i_T) and steady-state current (i_e) was 1.4 and 0.012 μA cm^{-2}, respectively, from the 0.5 V polarization of the cell. Using Equation 3, the ionic transport number could be estimated to $t_{ion}=0.99$, indicating that the conducting species are almost exclusively ionic.

A proof-of-concept all-solid-state magnesium battery was assembled to test $Mg(BH_4)_2 \cdot 1.5THF–MgO(75\ wt\%)$ as a solid-state electrolyte (Figure 5c). The cell was assembled with a magnesium metal anode and a cathode consisting of TiS_2 (75 wt%) and $Mg(BH_4)_2 \cdot 1.5THF–MgO(50\ wt\%)$ electrolyte (25 wt%) in a two-electrode configuration. The cell was assessed with galvanostatic cycling at C/50 and $T=55$ °C with a lower voltage limit of 0.2 V and a charging cut-off after 55 h. The initial discharge capacity of the cell was 94.2 mAh g^{-1}, which corresponds to $y=0.20$ in Mg_yTiS_2. In the subsequent cycles, the discharge capacity decreased below 60 mAh g^{-1}. All voltage profiles during charging was unsteady and fluctuating (Figure S13), which was not observed during discharge. To determine whether the fluctuation was due to the oxidation of the SS current collector, an additional cell with a Mo current collector was cycled with similar charging curves (Figure S14). This indicate that the fluctuation during charging occur between the electrolyte and the cathode. The first discharge profile displayed two voltage plateaus around 1 V and 0.6 V. A similar discharge profile has previously been reported for an intercalation of Mg^{2+} in layered TiS_2 where a Mg content of $y=0.56$ was intercalated during the first discharge with an additional voltage plateau at 1.2 V.[30] The absence of the voltage plateau at 1.2 V might be due to a self-discharge driven by the Mg^{2+} chemical potential across the electrolyte-cathode interface, which remains to be verified by a more detailed analysis. The battery performance may be further improved by the development of a protective cathode coating, which would

additionally expand the array of useable cathode materials for $Mg(BH_4)_2 \cdot x$THF–MgO nano-composites.

Conclusion

In summary, we investigate the crystal structures and electrochemical properties of the full range of magnesium borohydride tetrahydrofuran composites, and report three new compounds, α-$Mg(BH_4)_2 \cdot 2$THF, β-$Mg(BH_4)_2 \cdot 2$THF and $Mg(BH_4)_2 \cdot 2/3$THF. The crystal structures of the two $Mg(BH_4)_2 \cdot 2$THF polymorphs consist of molecular $[Mg(THF)_2(BH_4)_2]$ complexes, while detailed structural analysis of $Mg(BH_4)_2 \cdot 2/3$THF was unsuccessful. The distinct compounds, $Mg(BH_4)_2 \cdot x$THF ($x = 2/3$, 2, 3), displayed a higher Mg^{2+} conductivity as compared to $Mg(BH_4)_2$, but still too low for applications. However, composites formed between two distinct compounds, and stabilized by MgO nanoparticles, displayed a significant enhancement of the ionic conductivity. The mechanism for the high conductivity remain unknown, but likely show some resemblance to the $Mg(BH_4)_2 \cdot x$NH$_3$ composites described recently.[22,25,26]

Among the mechanically stable composites, the composition $Mg(BH_4)_2 \cdot 1.5$THF–MgO(75 wt%) displayed the highest conductivity of $\sigma(Mg^{2+}) \sim 10^{-4}$ S cm^{-1} at 70 °C. Lowering the MgO content to 50 wt% resulted in a softer pellet, but with extremely high conductivity of $\sigma(Mg^{2+}) \sim 10^{-2}$ S cm^{-1} at $T = 70$ °C. The conductivity, thermal and mechanical properties may be further optimized using other and smaller nanoparticles in different amounts, as demonstrated for LiBH$_4$.[31] Thus, hydride based materials has a large potential to achieve high ionic conductivities, also of divalent metals such as magnesium, at ambient temperatures. However, hybrid organic-inorganic materials are often relatively soft, which is a challenge for their utilization as solid-state electrolytes, where a static pressure is needed to keep electrodes and electrolyte in close contact. On the other hand, soft materials provide better deformability and therefor potentially keep good electrochemical contact in the cell during cycling.

This was demonstrated by a good Mg-anode compatibility, displayed in a symmetric Mg | $Mg(BH_4)_2 \cdot 1.5$THF–MgO(75 wt%) | Mg cell, showing stable plating/stripping for >100 cycles. Cyclic voltammetry revealed an oxidative stability of 1.2 V vs. Mg/Mg^{2+} and the highest reported coulombic efficiency (90%) among magnesium borohydride based electrolytes. The first rechargeable inorganic all-solid-state magnesium battery was assembled and cycled as a proof-of-concept using a TiS$_2$ cathode. The discharge capacity of the first cycle was 94.2 mAh g^{-1} when cycled at C/50 at 55 °C. This is the first report of a rechargeable inorganic all-solid-state magnesium battery. Thus, this research provides new insight into the development of magnesium batteries and the utilization of complex hydrides for solid-state electrolytes.

Experimental Section

Magnesium borohydride, α-$Mg(BH_4)_2$, was prepared according to previously described procedures.[32,33] Magnesium borohydride tetrahydrofuran, $Mg(BH_4)_2 \cdot 3$THF, was synthesized by dissolving α-$Mg(BH_4)_2$ in excess tetrahydrofuran (THF, OC_4H_8, anhydrous 99.9%, Sigma-Aldrich) at 20 °C, while stirring until all powder was dissolved. The mixture was subsequently dried under dynamic vacuum at room temperature using Schlenk-type equipment.

$Mg(BH_4)_2 \cdot x$THF ($x = 0.5$, 2/3, 1.0, 1.2, 1.3, 1.5, 1.7, 2.0, 2.5) were obtained by mixing α-$Mg(BH_4)_2$ and $Mg(BH_4)_2 \cdot 3$THF in appropriate ratios with subsequent mechano-chemically treatment. The powders were loaded into an 80 mL WC-coated vial with WC balls with a ball-to-powder weight ratio of 30:1 and milled 60 times at 350 rpm for 2 min, with a 2 min resting time between milling. Several composites ($0 \leq x \leq 2$) formed soft samples, and magnesium oxide nanoparticles, MgO (Sigma Aldrich, ≤ 50 nm) were added for mechanical stabilization in appropriate amounts (typically 75 wt%), see Table 1.

In-house powder X-ray diffraction (PXD) data were collected on a Rigaku SmartLab diffractometer with a Cu anode (Cu K_α radiation, 2 kW, $\lambda = 1.54056$ Å) at room temperature. In situ synchrotron radiation powder X-ray diffraction (SR-PXD) data were collected at the Paul Scherrer Institute (PSI) at beamline X04SA using $\lambda = 0.70870$ Å[34] and at the Diamond Light Source at beamline I11 using $\lambda = 0.826927$ Å. The samples were loaded in 0.5 mm borosilicate capillaries and sealed in argon atmosphere. The temperature was controlled using an Oxford cryostream.

The SR-PXD data were used for indexing and structural solution using the software FOX.[35] Subsequently, the structures were refined using the software Fullprof.[36] The BH$_4^-$ and C_4H_8O groups were treated as rigid bodies in FOX and using bond-length restraints in Fullprof. The background were described by linear interpolation between selected points, while Pseudo-Voigt profile functions were used to fit the diffraction peaks.

The structures of α- and β-$Mg(BH_4)_2 \cdot 2$THF from the Rietveld refinement were re-optimized by density functional theory (DFT) calculations. The DFT calculations were carried out using Vienna Ab-initio Simulation Package (VASP)[37] within the Perdew-Burke-Ernzerhof generalized-gradient approximation.[38] Projector augmented wave potential[39] with a planewave cut-off energy of 500 eV was used. Structural optimization was performed until the force on each atom became smaller than 0.005 eV/Å. A regular k-point grid of $3 \times 3 \times 2$ and $3 \times 3 \times 3$ was used for the α- and β-polymorphs, respectively; the k-point grid is dense enough to converge total energies within 0.1 meV per formula unit. The lattice parameters were optimized using higher planewave cut-off energy of 600 eV. Re-optimization of the experimental structural solution resulted in a minor rearrangement of the atomic positions and the calculated lattice parameters are close to the experimental values. The structural parameters are summarized in Table S1. The final Rietveld refinements of the DFT optimized structures using BH$_4^-$ and C_4H_8O as rigid bodies, resulted in minor changes in the atomic positions.

Temperature programmed photographic analysis was measured of samples sealed under argon in a glass tube and heated from 22 to 200 °C with a heating rate of 1 °C/min, while pictures were collected each 30 s.

Thermogravimetry and differential scanning calorimetry (TG-DSC) were measured with a PerkinElmer STA 6000. The samples (10–20 mg) were placed in an Al$_2$O$_3$ crucible in argon atmosphere and moved to the instrument with minimal exposure to air. A heating rate of 0.5 °C min^{-1} was used to heat the samples from 30 to 200 °C

in an argon flow of 30 mL min^{-1}. The outlet gases were analyzed simultaneously for hydrogen ($m/z = 2$) and THF ($m/z = 42$) with a Hiden Analytical HPR-20 QMS sampling system.

Electrochemical impedance spectroscopy (EIS) were measured with a BioLogic MTZ-35 impedance analyzer in a high temperature sample holder with Mo blocking electrodes. The samples were pressed into pellets at 3 T (0.9 GPa) with a diameter of 6.35 mm and a height of ~1 mm. The measurements were conducted under argon atmosphere and the temperature were measured by a K-type thermocouple. The samples were measured at 10 mV ac from 1 MHz to 1 Hz.

Cyclic voltammetry (CV) was recorded with a Biologic SP-300 in an in-house build PEEK cell, which was used as both die cast and electrochemical cell. A pellet with a diameter of 10.3 mm and a height of ~0.4 mm was pressed directly in the cell at 350 MPa with a Mg-electrode and a stainless steel (SS) electrode on each side. The Mg-electrode was polished with silicon carbide sandpaper right before assembly. A scan rate of 5 mV s^{-1} was used in the voltage range from −0.25 to 1.25 V for 100 cycles and an expanded voltage range for subsequent cycles.

The ion transport number, which is the fraction of the current due to the ions of the total current, was calculated from a chronoamperometry experiment, where a voltage of 0.5 V was applied to a symmetric cell with stainless steel (SS) blocking electrodes and monitoring the current response. The ion transport number was evaluated from the relation:

$$t_{ion} = \frac{i_{ion}}{i_T} = \frac{i_T - i_e}{i_T}, \tag{3}$$

where i_T is the total current response, i_e is the electronic current, and i_{ion} is the ionic current. The initial current response is the sum of the electronic and ionic current, and between two blocking electrodes the steady-state current is i_e.[40]

The galvanostatic cycling (GC) was similarly recorded at $T = 55\,°C$ with a Biologic SP-300 in an in-house build PEEK cell. The cell was assembled similar to the CV cell, where a cathode mix consisting of TiS$_2$ (Sigma Aldrich, 99.9%) and Mg(BH$_4$)$_2 \cdot$1.5THF—MgO(50 wt%) electrolyte was added opposite the Mg-electrode in a 75:25 wt% ratio, respectively. The cell was cycled at C/50 (44 μA cm^{-1}), assuming 2 e$^-$ per TiS$_2$, and with a lower voltage limit of 0.2 V and a charging cut-off after 55 h.

Further details of the crystal structure investigation(s) may be obtained from the Fachinformationszentrum Karlsruhe, 76344 Eggenstein-Leopoldshafen (Germany), on quoting the depository numbers CSD 2157929–2157930

Conflict of Interest

The authors declare no conflict of interest.

Data Availability Statement

The data that support the findings of this study are available in the supplementary material of this article.

[1] G. B. Alliance, in Geneva, Switzerland: World Economic Forum, **2019**.
[2] J. Liu, Z. Bao, Y. Cui, E. J. Dufek, J. B. Goodenough, P. Khalifah, Q. Li, B. Y. Liaw, P. Liu, A. Manthiram, Y. S. Meng, V. R. Subramanian, M. F. Toney, V. V. Viswanathan, M. S. Whittingham, J. Xiao, W. Xu, J. Yang, X.-Q. Yang, J.-G. Zhang, *Nat. Energy* **2019**, *4*, 180–186.
[3] C. Niu, H. Lee, S. Chen, Q. Li, J. Du, W. Xu, J.-G. Zhang, M. S. Whittingham, J. Xiao, J. Liu, *Nat. Energy* **2019**, *4*, 551–559.
[4] T. Famprikis, P. Canepa, J. A. Dawson, M. S. Islam, C. Masquelier, *Nat. Mater.* **2019**, *18*, 1278–1291.
[5] J. Janek, W. G. Zeier, *Nat. Energy* **2016**, *1*, 1–4.
[6] Z. Zhang, Y. Shao, B. Lotsch, Y.-S. Hu, H. Li, J. Janek, L. F. Nazar, C.-W. Nan, J. Maier, M. Armand, L. Chen, *Energy Environ. Sci.* **2018**, *11*, 1945–1976.
[7] F. Meng, J. McNeice, S. S. Zadeh, A. Ghahreman, *Miner. Process. Extr. Metall. Rev.* **2021**, *42*, 123–141.
[8] E. A. Olivetti, G. Ceder, G. G. Gaustad, X. Fu, *Joule* **2017**, *1*, 229–243.
[9] A. Alessia, B. Alessandro, V.-G. Maria, V.-A. Carlos, B. Francesca, *J. Cleaner Prod.* **2021**, *300*, 126954.
[10] L. Stievano, I. de Meatza, J. Bitenc, C. Cavallo, S. Brutti, M. A. Navarra, *J. Power Sources* **2021**, *482*, 228875.
[11] M. Fichtner, *Magnesium Batteries: Research and Applications*, The Royal Society of Chemistry, **2020**.
[12] R. Mohtadi, O. Tutusaus, T. S. Arthur, Z. Zhao-Karger, M. Fichtner, *Joule* **2021**, *5*, 581–617.
[13] R. Mohtadi, *Molecules* **2020**, *25*, 1791.
[14] M. Paskevicius, L. H. Jepsen, P. Schouwink, R. Černý, D. B. Ravnsbæk, Y. Filinchuk, M. Dornheim, F. Besenbacher, T. R. Jensen, *Chem. Soc. Rev.* **2017**, *46*, 1565–1634.
[15] K. T. Møller, D. Sheppard, D. B. Ravnsbæk, C. E. Buckley, E. Akiba, H.-W. Li, T. R. Jensen, *Energies* **2017**, *10*, 1645.
[16] A. Unemoto, M. Matsuo, S. Orimo, *Adv. Funct. Mater.* **2014**, *24*, 2267–2279.
[17] L. Duchêne, A. Remhof, H. Hagemann, C. Battaglia, *Energy Storage Mater.* **2020**, *25*, 782–794.
[18] E. Roedern, R.-S. Kühnel, A. Remhof, C. Battaglia, *Sci. Rep.* **2017**, *7*, 46189.
[19] T. Burankova, E. Roedern, A. E. Maniadaki, H. Hagemann, D. Rentsch, Z. Lodziana, C. Battaglia, A. Remhof, J. P. Embs, *J. Phys. Chem. Lett.* **2018**, *9*, 6450–6455.
[20] L. H. Jepsen, V. Ban, K. T. Møller, Y.-S. Lee, Y. W. Cho, F. Besenbacher, Y. Filinchuk, J. Skibsted, T. R. Jensen, *J. Phys. Chem. C* **2014**, *118*, 12141–12153.
[21] K. Kisu, S. Kim, M. Inukai, H. Oguchi, S. Takagi, S. Orimo, *ACS Appl. Mater. Interfaces* **2020**, *3*, 3174–3179.
[22] Y. Yan, W. Dononelli, M. Jørgensen, J. B. Grinderslev, Y.-S. Lee, Y. W. Cho, R. Černý, B. Hammer, T. R. Jensen, *Phys. Chem. Chem. Phys.* **2020**, *22*, 9204–9209.
[23] J. B. Grinderslev, M. B. Amdisen, L. N. Skov, K. T. Møller, L. G. Kristensen, M. Polanski, M. Heere, T. R. Jensen, *J. Alloys Compd.* **2021**, 163014.
[24] Y. Yan, J. B. Grinderslev, Y.-S. Lee, M. Jørgensen, Y. W. Cho, R. Černý, T. R. Jensen, *Chem. Commun.* **2020**, *56*, 3971–3974.
[25] Y. Yan, J. B. Grinderslev, M. Jørgensen, L. N. Skov, J. Skibsted, T. R. Jensen, *ACS Appl. Mater. Interfaces* **2020**, *3*, 9264–9270.
[26] Y. Yan, J. B. Grinderslev, T. Burankova, S. Wei, J. P. Embs, J. Skibsted, T. R. Jensen, *J. Phys. Chem. Lett.* **2022**, *13*, 2211–2216.

Batteries & Supercaps

Research Article
doi.org/10.1002/batt.202200163

Chemistry Europe
European Chemical
Societies Publishing

[27] E. B. Lobkovskii, L. V. Titov, S. B. Psikha, M. Yu. Antipin, Yu. T. Struchkov, *J. Struct. Chem.* **1983**, *23*, 644–646.

[28] O. Tutusaus, R. Mohtadi, N. Singh, T. S. Arthur, F. Mizuno, *ACS Energy Lett.* **2017**, *2*, 224–229.

[29] R. Mohtadi, M. Matsui, T. S. Arthur, S.-J. Hwang, *Angew. Chem. Int. Ed.* **2012**, *51*, 9780–9783; *Angew. Chem.* **2012**, *124*, 9918–9921.

[30] X. Sun, P. Bonnick, L. F. Nazar, *ACS Energy Lett.* **2016**, *1*, 297–301.

[31] V. Gulino, L. Barberis, P. Ngene, M. Baricco, P. E. de Jongh, *ACS Appl. Mater. Interfaces* **2020**, *3*, 4941–4948.

[32] Y. Filinchuk, B. Richter, T. R. Jensen, V. Dmitriev, D. Chernyshov, H. Hagemann, *Angew. Chem. Int. Ed.* **2011**, *50*, 11162–11166; *Angew. Chem.* **2011**, *123*, 11358–11362.

[33] B. Richter, J. B. Grinderslev, K. T. Møller, M. Paskevicius, T. R. Jensen, *Inorg. Chem.* **2018**, *57*, 10768–10780.

[34] P. R. Willmott, D. Meister, S. J. Leake, M. Lange, A. Bergamaschi, M. Böge, M. Calvi, C. Cancellieri, N. Casati, A. Cervellino, Q. Chen, C. David, U. Flechsig, F. Gozzo, B. Henrich, S. Jäggi-Spielmann, B. Jakob, I. Kalichava, P. Karvinen, J. Krempasky, A. Lüdeke, R. Lüscher, S. Maag, C. Quitmann, M. L. Reinle-Schmitt, T. Schmidt, B. Schmitt, A. Streun, I. Vartiainen, M. Vitins, X. Wang, R. Wullschleger, *J. Synchrotron Radiat.* **2013**, *20*, 667–682.

[35] V. Favre-Nicolin, R. Černý, *J. Appl. Crystallogr.* **2002**, *35*, 734–743.

[36] J. R. Carvajal, LLB Sacley & LCSIM Rennes, France, 2003.

[37] G. Kresse, J. Furthmüller, *Phys. Rev. B* **1996**, *54*, 11169–11186.

[38] J. P. Perdew, K. Burke, M. Ernzerhof, *Phys. Rev. Lett.* **1996**, *77*, 3865–3868.

[39] P. E. Blöchl, *Phys. Rev. B* **1994**, *50*, 17953–17979.

[40] S. Das, P. Ngene, P. Norby, T. Vegge, P. E. de Jongh, D. Blanchard, *J. Electrochem. Soc.* **2016**, *163*, A2029–A2034.